Randomized Aperture Imaging

Xiaopeng Peng,[1] Garreth J. Ruane,[1] and Grover A. Swartzlander, Jr.[1, *]

[1] *Rochester Institute of Technology, 54 Lomb Memorial Dr, Rochester, NY, 14623, USA*

Speckled images of a binary broad band light source (600-670 nm), generated by randomized reflections or transmissions, were used to reconstruct a binary image by use of multi-frame blind deconvolution algorithms. Craft store glitter was used as reflective elements. Another experiment used perforated foil. Also reported here are numerical models that afforded controlled tip-tilt and piston aberrations. These results suggest the potential importance of a poorly figured, randomly varying segmented imaging system.

arXiv:1601.00033v1 [astro-ph.IM] 1 Jan 2016

I. INTRODUCTION

It is well known that angular resolution may be enhanced by use of a larger aperture. In practice, the size of a monolithic aperture is limited by the cost, weight and construction constraints[1, 2]. Even if such constrains can be surmounted, adaptive optics methods must be applied to achieve diffraction limited performance[3]. Alternatively, passive approaches that make use of computer post-processing have been successfully employed[4–6]. Examples, including an aperture masking system[7], and a multi-aperture system[8] have shown great promise in astronomy and remote sensing[9–11], biology[12], clinical trials[13, 14], and new types of computational cameras[15–17]. In these imaging systems, the burden of hardware control are replaced or greatly alleviated by digital computations. Mathematical tools, such as Fourier analysis[18], constrained optimization[19, 20], and Bayesian inference[21] are essential in this approach. Both aperture masking and multi-aperture systems have demonstrated an improved signal-to-noise ratio of the acquired images, a calibrated point spread function (PSF), rejection of atmospheric noise, and closure phase measurements[22]. However, the sparsity of apertures implies a sparse coverage of spatial frequencies and loss of flux. Both adaptive optics and aperture masking systems attempt to improve the images obtained from a relatively well-figured optical system. In this paper we address the case of an ill-figured segmented optical system that varies randomly in time. To make matters worse, we assume no knowledge of the randomly varying PSF. We ask the following the proof of concept question: Is it possible to reconstruct a near diffraction-limited image from a series of recordings from such a system?
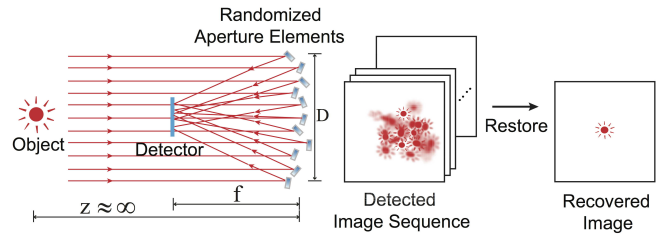

FIG. 1. Random aperture imaging system having baseline D, depicting a distant light source, random elements, and a detector in an effective focal plane. A sequence of images are recorded for different random orientations of the elements. Computational imaging methods are used to reconstruct the image of the light source.

In some respects this study is related to the random lens imaging system[23], where a collection of random reflectors served as a primary camera lens. Similarly, the sparkle vision system[24], simplifies the random lens imaging system by using a lens to better focus the light. However, in these examples, the PSF was not time-varying, and intensive machine learning algorithms were needed to uncover the PSF. In contrast, we aimed to reconstruct the time-varying PSF in a near real-time manner.

This report is organized as follows. In Section 2 we provide a description of a randomized complex aperture system. Two different experimental scenarios are established in Section 3: "far field" and "near field". For the purpose of comparing experimental and modeled results, we next describe in Section 4 the corresponding numerical models. Both the experimental and numerical data are processed by means of the multiframe blind deconvolution scheme described in Section 5. We then report image construction results in Section 6. Concluding remarks are provided in Section 7.

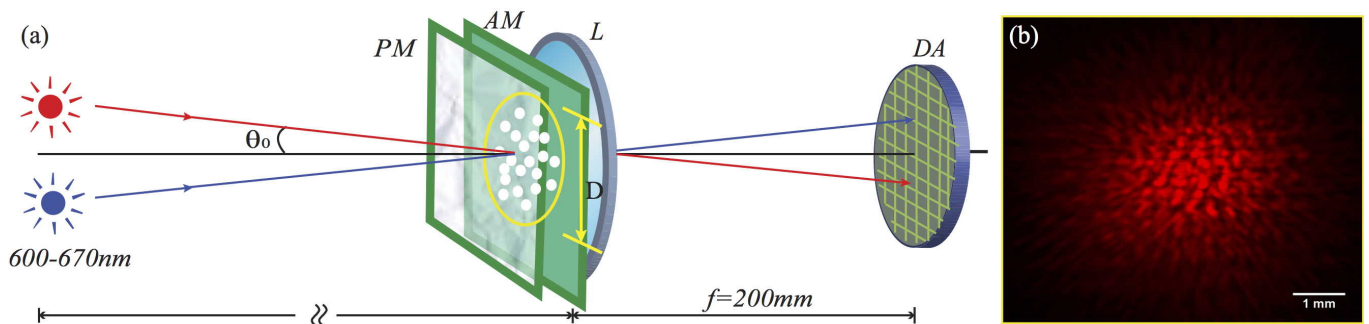* Corresponding author: gaspci@rit.edu

FIG. 2. Configuration of the far field experiment. (a)Two polychromatic sources subtend an angle θ_0 with respect to the optical axis. Rays are transmitted though a phase mask (PM) and aperture mask (AM) near the front face of a lens L of focal length $f = 200mm$. Using different random masks, multiple images are recorded on the detector array (DA), placed in the Fourier transform (back focal plane) of the lens. (b) Example of a recorded image from a random mask.

II. BASICS OF RANDOMIZED APERTURE IMAGING

An illustration of the randomized aperture scheme, shown in Fig. 1, depicts a point source (or sources) an infinite distance from elements that are distributed across a quasi-parabolic surface of baseline D and a detector at the mean focal distance f. For a continuous parabolic reflector, a diffraction-limited image would appear on the detector. However, tip,tilt and piston errors associated with each reflecting element produces aberrated speckles. Further, the distribution may be evolving in time, providing a sequence of N speckled images. Here, we ignore motion blur. Postprocessing techniques such a multi-frame blind deconvolution [25–28] may be used to recover a near-perfect image. This approach is particularly suitable in cases where it is not practical to make repeated measurement of time varying PSF. What is more, multi-frame blind deconvolution is a self-heuristic algorithm with less computational cost than machine learning, and may be simpler to implement than phase retrieval methods when the PSF is time varying. An advantage of this approach is (see Section 5) that whereas a single-image blind deconvolution scheme prescribes a ratio of unknowns (the PSF and the recovered object) to measurements as $2:1$, the multi-frame blind deconvolution scheme improves the ratio to $N+1:N$. In general, the system shown in Fig. 1 may be shift-variant, in which case shift-variant multi-frame blind deconvolution algorithms[27] are better suited. For the cases examined below, however, the small shift-variance may be neglected, and we find the shift-invariant multi-frame blind deconvolution algorithm is sufficient to achieve good reconstructed image of a pair of point sources.

III. LABORATORY DEMONSTRATION

Far Field. In the case shown in Fig 2, a "far field" arrangement was constructed whereby a transmissive mask was positioned at the surface of a convex lens of focal length $f = 200mm$. A set of $N = 50$ thin foil masks was produced, each having $M = 50$ randomly placed pinholes(radius $r \approx 0.1mm$) distributed across a $D = 3mm$ diameter. The foil was covered by a layer of wrinkled cellophane to randomize the phase at each pinhole. The close proximity of the cellophane and foil allowed for a nearly shift-invariant system. An Energetiq laser-driven white light source was spatially and spectrally filtered to produce a collimated polychromatic beam with a wavelength range $\lambda = 600 - 670nm$. Light transmitted through the mask was recorded at the back focal plane of the lens on the detector array of a Canon 5D Mark III camera having a pixel pitch of $6.25\mu m$ and detector size of $24\times36mm$. We call this arrangement "far field" because the detected light is governed by Fraunhofer diffraction from the pinholes. Imaging information is encoded in the interference of the diffracting beamlets. An effective second mutually incoherent light source was introduced by transmitting the beam through the system at angle $2\theta_0$. The two images were added together to produce a single image of a binary source. The ground truth image can be obtained using the same setup, but without the phase and aperture masks.

Near Field. A schematic of the second experimental setup is shown in Fig 3. for a "near field" arrangement. As above, spatially and spectrally filtered light was formed into a collimated beam. In this case, however, reflecting elements were used to divert beamlets toward the detector. We used the front surface reflection from a glass wedge to produce a binary light source. The reflecting elements were comprised of square "fine size" craft store glitter, with dimensions of roughly $0.3\times0.3mm$. The random aperture condition was achieved by randomly sprinkling glitter across a blackened concave surface having a radius of curvature $65.4mm$. After each image was recorded, the glitter was washed off, and a new random surface was prepared. The number of sub-apertures across the full $D = 10mm$ beam diameter ranged from $M = 200$ to 400. The pellicle beam splitter was used
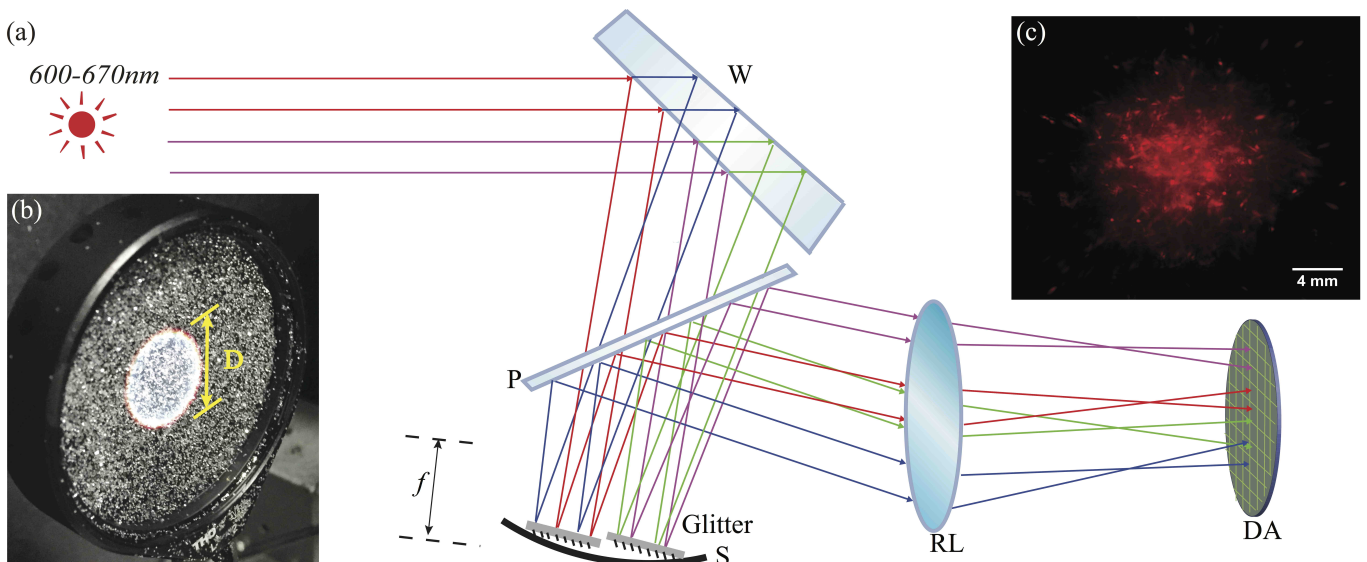
FIG. 3. Configuration of the near field experiment. (a) A glass wedge (W) is used to create a double image of a single polychromatic light source. The rays are reflected from randomly distributed glitter across a blackened concave surface (S) having a radius of curvature $65.4mm$. A Pellicle beam splitter (BS) direct the rays through a lens (L), which acts to relay the image at the focal plane, to the detector array (DA). (b) Photograph of the random glitter surface having an effective diameter, D. (c) Example of a recorded image of the binary source from a random glitter surface. Multiple random images were recorded by removing and then re-applying glitter.

to collect the reflected light and direct it toward the detector array of the same camera. Owing to space constraints, the detector could not be placed directly in the focal plane of the concave surface ($f = 32.7mm$ from the surface), and thus, a $150mm$ relay lens was used. This configuration is called "near field" because the beamlets from each reflecting element undergo Fresnel diffraction upon reaching the detector. The diffraction length of a single reflecting element is roughly $450mm$, which is much greater than f. We assert that the system is nearly shift invariant since the elements roughly conform to a small patch of diameter D on the concave surface. As seen in the inset of Fig. 3, the elements display significant tip-tilt errors.

The reconstruction results of experimental data are discussed in Section 6. Parameters of both schemes are listed in Table 1.

IV. NUMERICAL SIMULATION OF OPTICAL SYSTEM

Far Field. A numerical model of the far field experiment may be represented by a distribution of complex circular sub-aperture functions (see Fig 4):

$$U_i(\mathbf{x}) = exp\left(|\tilde{\mathbf{x}}_{\mathbf{i}}|\right)^{\beta} exp(i\phi_i) \tag{1}$$

where $\tilde{\mathbf{x}}_{\mathbf{i}} = |\mathbf{x} - \mathbf{c}_i|_2/r_s$ is a normalized vector, $\mathbf{x} = (x, y)$ is an arbitrary vector in the plane of the aperture, $\mathbf{c_i} =$

TABLE I. Values of Experimental Parameters

Parameter	Far Field	Near Field
Number of sub-apertures in the cloud M	50	200-400
Diameter of the baseline D[mm]	3	10
Size of sub-aperture [mm]	0.2	0.3
Focal length f[mm]	200	32.7
Samples per $\lambda F\#$ in image plane[pix]	7	0.4
Angular Separation of sources λ/D	26	625
Bandwidth [$\Delta\lambda$]	%10	%10
Detector array size[mm^2]	24 x 36	
Detector pixel pitch [μm]	6.25	

$(c_{x,i}, c_{y,i})$ indicates the center of the i-th sub-aperture, r_s is the radius of the sub-apertures, $|\cdot|_2$ is l^2-norm, and $\beta = 100$ is the power of Super-Gaussian function that defines the sub-apertures.

Phase aberrations, $\phi_i = \phi_{p,i} + \phi_{t,i}$, across each sub-aperture are represented, respectively, by piston and tip-tilt terms:

$$\phi_{p,i}(\mathbf{x}) = ka_i \tag{2}$$

$$\phi_{t,i}(\mathbf{x}) = k\mathbf{x}\mathbf{b}_i \tag{3}$$

where $k = 2\pi/\lambda$ is wavenumber, a_i is a pairwise independent uniformly distributed random variable with in-
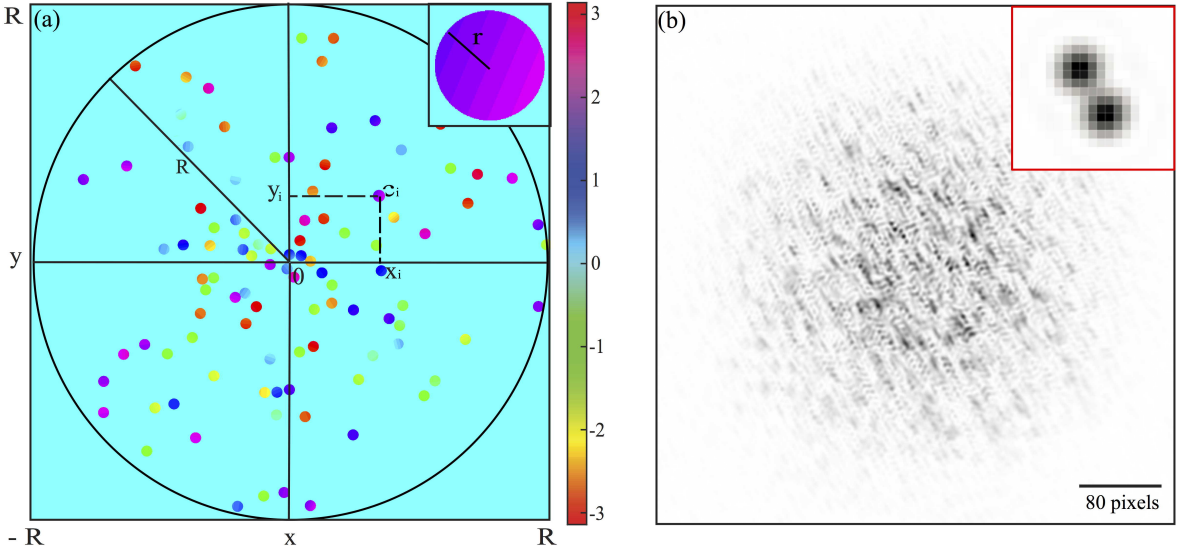
FIG. 4. Numerical model of the far field scheme. (a) Sub-apertures of radius r (small circles) are distributed across the baseline radius $D = 2R$ on an $N \times N$ grid ($N = 8192$). The transmitted light has a Gaussian random tip-tilt phase (with standard deviation up to $40\lambda/D$ across the diameter $D = 2R$), as well as a uniformly distributed piston error of up to one wave. The $M = 100$ non-overlapping randomly placed sub-apertures are assigned a position $\mathbf{c_i} = (x_i, y_i)$. (b)Numerical image of a binary light source at the Fourier transform plane. The image has been inverted to aid the eye.

terval equals to Δz, $\mathbf{b}_i$ is a pairwise independent Gaussian random variable with mean 0 and variance given by $< a_i^2 >= \sigma_0^2$, and $< - >$ denotes an ensemble average.

The complete system aperture function may be expressed as

$$U(\mathbf{x}) = \left[\sum_{i=1}^{M} U_i(\mathbf{x}) \right] exp \left(\frac{|\mathbf{x} - \mathbf{c}_0|_2}{R} \right)^\gamma \qquad (4)$$

where M is the number of sub-apertures, $\mathbf{c}_0 = (c_{x,0}, c_{y,0})$ indicates the center of the baseline, and R the radius of the full effective aperture, and $\gamma = 100$ is the power of Super-Gaussian function that defines the baseline.

We further impose a non-overlapping condition to the sub-apertures:

$$|\mathbf{c}_i - \mathbf{c}_j| > 2r_s, i \neq j \qquad (5)$$

An example of the complex pupil function is shown in Fig 4.(a) for $M = 100$ sub-apertures.

For two monochromatic point sources at infinity having an apparent angular separation of $2\theta_0$ along the x-direction, the electric field in the back focal plane of the system may be expressed as Fourier transforms of the field from each source, incident upon the imaging system(assuming it is shift-invariant):

$$E^+(\mathbf{v}) = \frac{1}{\lambda} \sum_{\mathbf{x}} exp \left(i\frac{2\pi}{\lambda}\mathbf{v} \cdot \mathbf{x} \right) U(\mathbf{x}) exp(+ik_x\mathbf{x}) \qquad (6)$$

$$E^-(\mathbf{v}) = \frac{1}{\lambda} \sum_{\mathbf{x}} exp \left(i\frac{2\pi}{\lambda}\mathbf{v} \cdot \mathbf{x} \right) U(\mathbf{x}) exp(-ik_x\mathbf{x}) \qquad (7)$$

where for paraxial rays, $k_x \approx 2\pi\theta_0/\lambda$.

Assuming the two light sources are mutually incoherent, we write the intensity in the plane of the detector as:

$$I(\mathbf{x}) = |E^+|^2 + |E^-|^2 \qquad (8)$$

Near Field In the near field regime, the numerical model ignores diffraction of the reflected light as it propagates from the aperture to the focal plane detector. That is, we assume the characteristic diffraction distance is much longer than the effective focal length: $\pi r_s^2/\lambda >> f$.

The geometric model of near field scheme is illustrated in Fig 5. For a single source of collimated light, we assume a beam of parallel ray aligned along the unit vector $\mathbf{d}_0$. Rays incident upon the i_{th} reflector centered at the point $\mathbf{c}_i$ are reflected along the unit vector $\mathbf{d}_{r,i}$:

$$\mathbf{d}_{r,i} = \mathbf{d}_0 - 2\left(\mathbf{d}_0 \cdot \mathbf{n}_i \right) \mathbf{n}_i \qquad (9)$$

where the Cartesian components of the unit normal vector of the i_{th} reflector may be expressed in terms of direction cosines as: $\mathbf{n}_i = (\cos\theta_i)$, where $\theta_i = (\theta_{x,i}, \theta_{y,i}, \theta_{z,i})$.

If the reflectors conformed to a paraboloid

$$z = -(x^2 + y^2)/4f + f \qquad (10)$$

where f is the focal length. Each of the i_{th} rays directed along $\mathbf{d}_{r,i}$ would coincide at the focal point $\mathbf{o} = (0, 0, 0)$. In that special case the direction angles of the normal vector of each reflector may be expressed as $\theta_{i,0} = (\theta_{x,i,0}, \theta_{y,i,0}, \theta_{z,i,0})$, where
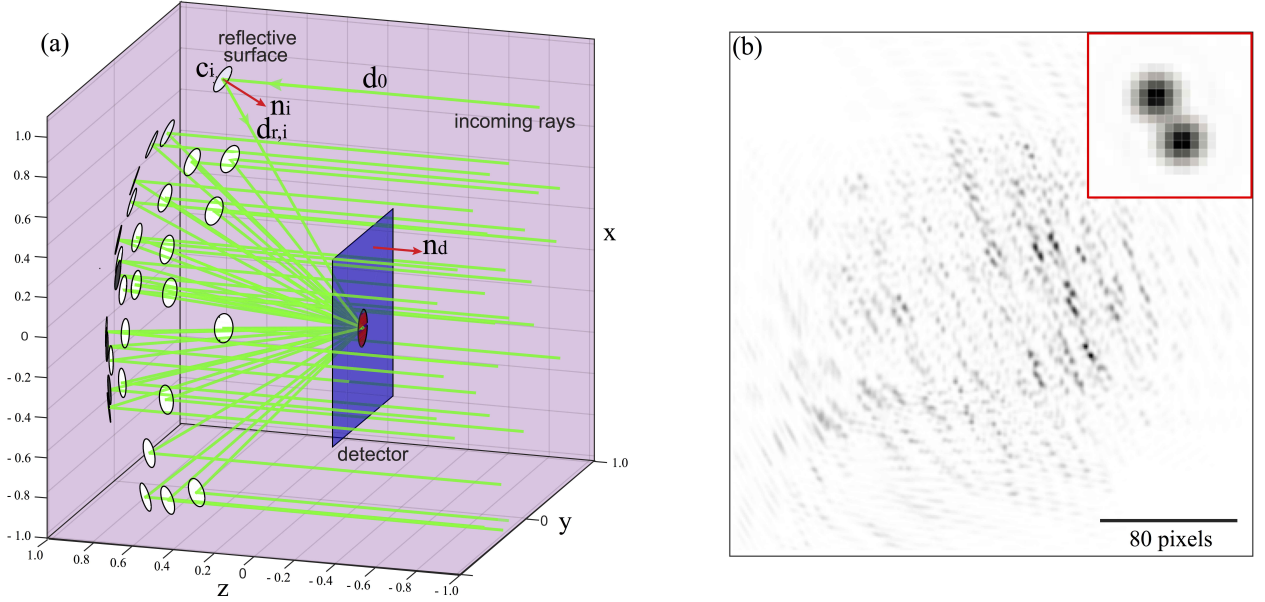
FIG. 5. Numerical model of the near field scheme. (a) Randomly distributed circular reflecting elements of radius $r = 100$ pix at the points $\mathbf{c}_i = (x_i, y_i, z_i)$ are aligned along a parabolic surface with $F\# = 75$, each provided with random tip-tilt (with standard deviation up to $60\lambda/D$ across the diameter $D = 20000$ pix), as well as a uniform piston error of up to ten waves. Incoming collimated rays directed along the unit vector $\mathbf{d}_0$ are assumed to reflect in the direction $\mathbf{d}_{r,i}$ without diffracting as they propagate to the focal plane detector array. Respective element and detector surface normals: $\mathbf{n}_i$ and $\mathbf{n}_d$. (b) Example of a numerical image of a binary light source at the focal plane.

$$\theta_{x,i,0} = cos^{-1}(x/2pf)$$
$$\theta_{y,i,0} = cos^{-1}(y/2pf) \qquad (11)$$
$$\theta_{z,i,0} = cos^{-1}(1/p)$$

and $p = ((x/2f)^2 + (y/2f)^2 + 1)^{1/2}$. We note theses angles are related by $cos^2(\theta_{x,i,0}) + cos^2(\theta_{y,i,0}) + cos^2(\theta_{z,i,0}) = 1$.

In general, the normal vector of each reflector will suffer from random tip-tilt errors $\boldsymbol{\Delta\theta_i} = (\theta_{x,i}\Delta a_{x,i}a_{y,i}\Delta\theta_{y,i}, a_{z,i}\Delta\theta_{z,i})$, and thus the directional angles becomes

$$\theta_i = \theta_{i,0} + \boldsymbol{\Delta\theta_i} \qquad (12)$$

where $a_{x,i}, a_{y,i}, a_{z,i}$ are pairwise independent Gaussian random variables variable with mean 0 and variance equal to σ_0.

Piston error, $w_i \Delta z_i$ may be introduced by displacing the center of the i_{th} mirror from the paraboloid surface defined by $\mathbf{c}_i = (c_{i,x}, c_{i,y}, f + (c_{i,x}^2 + c_{i,y}^2)/4f)$, where w_i is pairwise independent uniform random variable with interval of Δz_i

Let us consider a ray incident upon an arbitrary point $\mathbf{x} = (x, y, z)$ on the i_{th} flat reflecting element. The plane of the element is represented by the equation $\mathbf{n}_i(\mathbf{x} - \mathbf{c}_i) = 0$. For a circular reflector of radius r_s we impose $|\mathbf{x} - \mathbf{c}_i|^2 \leq r_s^2$. The intersection points of the incident beam with the plane of the i_{th} circular reflector can be represented parametrically as:

$$\mathbf{m}_i = \mathbf{c}_i + \alpha \cos t \mathbf{e}_1 + \alpha \cos t \mathbf{e}_2 \qquad (13)$$

where $t \in [0, 2\pi]$, $\alpha \in [0, r_s]$, $\mathbf{e}_1$ and $\mathbf{e}_2$ are unit vectors that satisfy $\mathbf{e}_1 = (0, 1, cos\theta_x/cos\theta_y)/(1 + (cos\theta_x/cos\theta_y)^2)^{1/2}$ and $\mathbf{e}_2 = \mathbf{e}_1 \times \mathbf{n}$.

Next we wish to determine where the reflected beam intersects the detector plane. In general, the detector plane can be defined by a center point $\mathbf{q}$ (usually the focal point of the paraboloid) and a normal vector $\mathbf{n}_d$. The projection of the points $\mathbf{m}$ along the reflected beam onto the detector plane may then be expressed as:

$$\mathbf{u}_i = \mathbf{m}_i + \mathbf{d}_r \frac{(\mathbf{q} - \mathbf{m}_i) \cdot \mathbf{n}_d}{\mathbf{d}_r \cdot \mathbf{n}_d} \qquad (14)$$

The electric field within each of the i_{th} projected beams in the detector plane may be represented as a tilted plane wave scaled by an obliquity factor from both the mirror $\mathbf{d}_0 \cdot \mathbf{n}_i$, and the detector $\mathbf{d}_r \cdot \mathbf{n}_d$.

With two point sources at infinity, we repeat the above procedure by including two bundles of incoming rays reflected from an element along unit vectors $\mathbf{d}_0^+$ and $\mathbf{d}_0^-$ respectively. The two fields in the detection plane are labelled E_i^+ and E_i^-:

$$E^+(\mathbf{u}_i^+) = A_i^+ exp(ik\mathbf{d}_{r,i}^+ \cdot \mathbf{u}_i^+)exp(ikL_i^+)$$
$$E^-(\mathbf{u}_i^-) = A_i^- exp(ik\mathbf{d}_{r,i}^- \cdot \mathbf{u}_i^-)exp(ikL_i^-) \qquad (15)$$

TABLE II. Value of Numerical Parameters

Parameter	Far Field	Near Field
Image plane grid size [pix]	4096	4096
Radius of sub-aperture $2r$[pix]	82	100
Diameter of the baseline D[pix]	8092	20000
Pixels per $\lambda F\#$ in image plane	4	7.5
Angular separation of the objects[λ/D]	1.5	1.5

where A_i^+ and A_i^- are zero valued outside the projection area of the i_{th} mirror. L_i^+ and L_i^- are full path length of rays that travel from the binary source to the i_{th} mirror, and then reflected onto the detector. $k = 2\pi/\lambda$ is the wavenumber. For small angular deviations in the detector plane and for equally luminous point sources, we make the approximation of setting the A_i^+ and A_i^- within the interior regions of each bundle of rays equal for all $\mathbf{u}_i$. Here we consider two mutually incoherent sources subtending an angle $2\theta_0$ and bisecting the z-axis: $\mathbf{d}^+ \cdot \mathbf{d}^- = cos(2\theta_0)$. Defining the postion vector on detector plane as $\mathbf{x}_d = (x_d, y_d)$, the measured irradiance may be expressed:

$$I(\mathbf{x}_d) = |\sum_{i=1}^{M} E_i{}^+(\mathbf{x}_d)|^2 + |\sum_{i=1}^{M} E_i{}^-(\mathbf{x}_d)|^2 \quad (16)$$

The ground truth image is captured by imaging the objects using a monolithic mirror of the baseline size. The value numerical parameters are given in Table 2.

V. SYSTEM ESTIMATION AND IMAGE RECOVERY

Multi-frame blind deconvolution algorithms are used to recover a target scene from a set of blurry, noisy and distorted observations. They are generally categorized into two types: (1) non-blind deconvolution, where the target scene is reconstructed based on complete or partial knowledge of the point spread function(PSF) of the imaging system; and (2) blind deconvolution, where the unknown target scene and system point spread function are recovered simultaneously without a priori knowledge. Since the work of Ayers and Dainty[29], multi-frame blind deconvolution has become an important tool for image recovery, resulting in numerous research efforts and applications. Common approaches involve: (1) Batch mode multi-frame blind deconvolution[25, 30], where all the distorted observations are processed at the same time; and (2) Serial mode multi-frame blind deconvolution[26, 31, 32], where degraded inputs are sequentially processed. Compared with the batch mode, the serial approach is more memory efficient and can in principle be done at the same time as the image acquisition. In this paper image restoration was accomplished by use of a serial multi-frame blind deconvolution[31] scheme.

Here we give a brief review of the online multi-frame blind deconvolution algorithm. We assume that at each time point $n = 1, 2, \cdots, N$, the random aperture mirror system records a blurred image $\{g_n\}$. Assuming the imaging system is shift-invariant(or approximate shift-invariant), the image formation process can be modeled as convolution of the target image and the system PSF, where the recorded n_{th} image $g_n(x, y)$ may be expressed:

$$g_n = (f \otimes h_n) + q_n \quad (17)$$

where $\otimes$ denotes the two-dimensional convolution operator, and $f(x, y)$ and $q_n(x, y)$ respectively represent the ideal image and its random noise, and $h_n(x, y)$ represents the shift-invariant PSF of the n_{th} time frame. We assume the PSF changes from frame to frame owing to time varying tip, tilt, and piston errors, as well as the location of each mirror. The goal for multi-frame blind deconvolution is to recover the ideal image f and the temporally varying PSF h_n from a set of degraded images $\{g_n\}$. A simple but effective choice for the blind deconvolution can be achieved by solving the following non-negatively constrained problem [26]

$$\{f, h_n\} = \min_{h_n \geq 0, f \geq 0} \frac{1}{N^2} \sum_{n=0}^{N} \sum_{\mathbf{u}} |G_n - \tilde{F}\tilde{H}_n|^2(\mathbf{u}) \quad (18)$$

where $\tilde{G}_i, \tilde{F}, \tilde{H}_i$ are the Fourier transforms of the observed images g_i, ideal image f, and PSFs h_i respectively, and $\mathbf{u}$ is the position vector in frequency space.

Solutions to Eq.18 are commonly solved using either: (1) batch mode optimization using the constrained conjugate gradient descent of cost function with respect to f and $\{h_n\}$ in an alternating manner[25, 28, 30]; and (2) serial mode optimization using the multiplicative updates[26, 31], as is shown in the method we employed, outlined below in Algorithm 1,estimated image and PSF are updated respectively using multiplicative method in each iteration:

$$H_i = H_{i-1} \odot \frac{F_i^T G_i}{F_i^T(F_i H_{i-1})} \quad (19)$$

$$F_i = F_{i-1} \odot \frac{H_i^T G_i}{H_i^T(H_i F_{i-1})} \quad (20)$$

and where $\odot$ denote the component-wise multiplication.

Algorithm 1: Alternating Minimization for Online Blind Deconvolution

---

Input: Captured image sequence $\{G_n\}$
Output: Restored image F and PSFs $\{H_n\}$
Initialize $F = F_0$, H_0
$i = 1$
while $\sum_{\mathbf{u}} |G_i - FH_i|^2 > \epsilon$ *and* $i < N$ **do**
   $H_i = \arg\min \sum_{\mathbf{u}} |G_i - F_{(i-1)}H|^2$
   $F_i = \arg\min \sum_{\mathbf{u}} |G_i - FH_i|^2$
   $i = i + 1$
   $F = F_i$
end

VI. RESULTS AND DISCUSSION

Analyses of our reconstructed images resulting from multi-frame blind deconvolution are presented below. First we describe the experimentally measured data for far field and near field schemes using a polychromatic (10% bandwidth) light source. Numerically generated data is then used to demonstrate the reconstruction of a monochromatic binary light source under different tip-tilt and piston errors. Quantitative comparisons between ground truth and reconstructed images are evaluated based on two metrics: spatial separation error $E_D = |D - D'|/D$ and the peak intensity ratio error $E_p = |I_{p,1}/I_{p,2} - I'_{p,1}/I'_{p,2}|/(I_{p,1}/I_{p,2})$, where D and D' are the respective distances between the peaks of the ground truth and restored images respectively, and where I_p and I'_p are the respective peak intensities of the ground truth and restored results.

A. Experimental Results

Reconstructed images were obtained by use of $N = 50$ images for both the far field and near field schemes. Details of the experimental setup and parameters are discussed in Section 4 and Table 1. The restored images of a binary light source and examples of speckle images are shown in Fig 6. Immediately we see in both cases that the reconstructed images are superior to the speckle images, i.e, qualitative agreement with the ground truth is acheived. Quantitatively, we find the distance between the intensity peaks are in good agreement, with $E_D \approx 5\%$. Furthermore the intensity peaks are equal to within $E_p \approx 15\%$. This is remarkable considering the 10% bandwidth of the light source, and the estimated $15\lambda/D$ tip-tilt error and a likely piston error of at least several waves. The good agreement between the ground truth and reconstructed images may be attributed to the high degree of shift invariance of the imaging systems. That is, the speckle data in both Fig 6.(b) and (d) contains multiple overlapping pairs of binary images. We note that in the far field (diffracted) case the pairs dis-

placed from the central region of the speckle image are diffused owing to the broad bandwidth of the light source. In contrast, for the near field case, the beamlets from each reflecting element experience little diffraction, and thus no chromatic spreading of the beamlets. We believe the multiframe BD scheme is successful at recovering the binary light source in both cases because the underlying imaging systems are well described by a shift invariant convolution process.

B. Numerical Results

To explore how well multiframe blind deconvolution restores a binary image from random aperture mirror images, numerically simulated far field and near field data were generated for various degrees of tip-tilt and piston error. Details of the system were described in Sec 4 and Table 2.

First we examine numerical cases that closely resemble the experimental system. For both the near and far field schemes we numerically generated speckled images with 50 non-overlapping sub-apertures. Gaussian random tip-tilt error with $\sigma_0 = 10\lambda/D$ and uniform random piston error with $\Delta z = 1\lambda$ were assumed for each of the $N = 60$ images of the generated sequence. Shown in Fig 7 are the ground truth and example speckle images for the far field and near field scenarios. The insets show a zoomed image of the ground truth in Fig 7.(a), and the corresponding reconstructed images in Fig 7.(b,c). As in the experimental case, the qualitative agreement between the ground truth and reconstructed images is good. Quantitatively the spatial separation error is $E_D \approx 10\%$ for both cases, and the magnitude ratio error is E_p is less than 4%. These errors are smaller than the experimental values because the numerical cases are noise free and monochromatic. We found that the near field values of E_D and E_p are somewhat larger than the far field values. We attributed this difference to the lower degree of shift invariance in the near field case owing to different projections of the beamlets on the detector plane.

To examine the fidelity of reconstructed image as a function of tip-tilt and piston error, we modeled the far field system with $\sigma_0 = 10, 20, 40[\lambda/D]$ with no piston error (see Fig 8), and then $\Delta z = 0.5, 1.0, 1.5\lambda$ with no tip tilt error (see Fig 9). In these cases we set the number of sub-apertures to $M = 100$, and the number of images to $N = 50$. As expected, the quality of the reconstructed images deteriorates with increasing phase error. The reconstruction errors increase from $E_D \approx 8.9, 9.1$ to 9.4%, and $E_P \approx 2, 24$ to 34% as the tip-tilt error increase from $\sigma_0 = 10$ to 20 to $40[\lambda/D]$. On the other hand, as the increment of piston error increases from $\Delta z = 0.5$ to 1.0 to 1.5λ, the errors for the restoration increase from $E_D \approx 13, 16$ to 22%, and E_P increase from $\approx 6, 27$ to 58%. For both tip-tilt and piston error we find the magnitude ratio error suffers more significantly than the spatial separation error. We attribute this to the increased
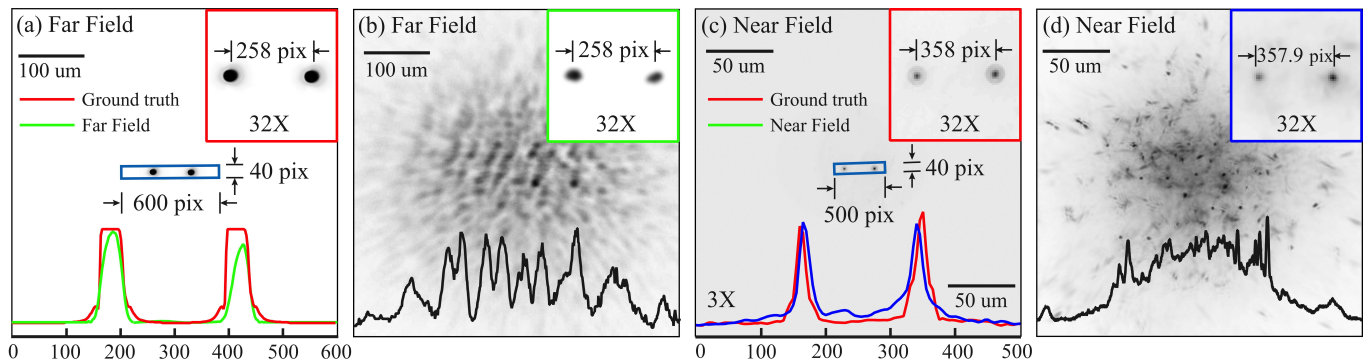
FIG. 6. Image reconstruction results of multi-frame blind deconvolution applied to an experimental far field sequence and an experimental near field sequence respectively(polychromatic with band width $\Delta\lambda/\lambda = 10\%$). The far field sequence is obtained with $M = 50$ non-overlapping sub-apertures, and the near field sequence is obtained with $M \approx 200 - 400$ non-overlapping reflecting elements. The tip-tilt error in near field sequence is approximate to $15\lambda/D$ (a)Groundtruth image of the binary light sources in far field scheme, and the comparison of the line profile of the ground truth and the recovered result; (b)A typical image in the captured far field sequence and the enlarged part of the recovered result; (c)Groundtruth image of the binary light sources in near field scheme, and the comparison of the line profile of the ground truth and the recovered results; (d)A typical image in the captured near field sequence and the enlarged part of the recovered result;

intensity of speckles and interference patterns that are resulted from sufficiently large phase errors.

VII. CONCLUSION

We numerically and experimentally explored the concept of random aperture mirror telescope for both monochromatic binary light sources and polychromatic binary light sources, in both far field and near field schemes. For an approximate shift-invariant system, binary light sources can be restored using Multi-frame blind deconvolution techniques from both experimental and numerical data with reconstruction error kept in a tight tolerance. The numerical results further demonstrate that for an approximate shift-invariant system, a near diffraction limit resolution ($1.5\lambda F\#$) can be achieved in the presence of tip-tilt of $40\lambda/D$ and piston phase up to 1.0λ for monochromatic sources.

Several interesting aspects remain yet to be analyzed.

We would like to quantifying the phase errors by the use of spatial light modulator in the experiments. Also, further investigation of a few system parameters, i.e. fill factor of sub-apertures, varying $F\#$, the number of light sources, the magnitude ratio among sources, as well as noise will be conducted for both experiments and numerical simulation to better evaluate the system performance.

VIII. ACKNOWLEDGMENT

[1] A. B. Meinel, "Cost-scaling laws applicable to very large optical telescopes," Optical Engineering **18**, 645–647 (1979).

[2] G. T. Van Belle, A. B. Meinel, and M. P. Meinel, "The scaling relationship between telescope cost and aperture size for very large telescopes," in "SPIE Astronomical Telescopes+ Instrumentation," (International Society for Optics and Photonics, 2004), pp. 563–570.

[3] G. Chanan, D. G. MacMartin, J. Nelson, and T. Mast, "Control and alignment of segmented-mirror telescopes: matrices, modes, and error propagation," Applied Optics **43**, 1223–1232 (2004).

[4] A. Labeyrie, "Attainment of diffraction limited resolution in large telescopes by fourier analysing speckle patterns in star images," Astron. Astrophys **6**, 85–87 (1970).

[5] J. R. Fienup, "Phase retrieval algorithms: a personal tour [invited]," Applied Optics **52**, 45–56 (2013).

[6] S. Chaudhuri, R. Velmurugan, and R. Rameshan, "Blind deconvolution methods: A review," in "Blind Image Deconvolution," (Springer, 2014), pp. 37–60.

[7] E. Caroli, J. Stephen, G. Di Cocco, L. Natalucci, and A. Spizzichino, "Coded aperture imaging in x-and gamma-ray astronomy," Space Science Reviews **45**, 349–403 (1987).
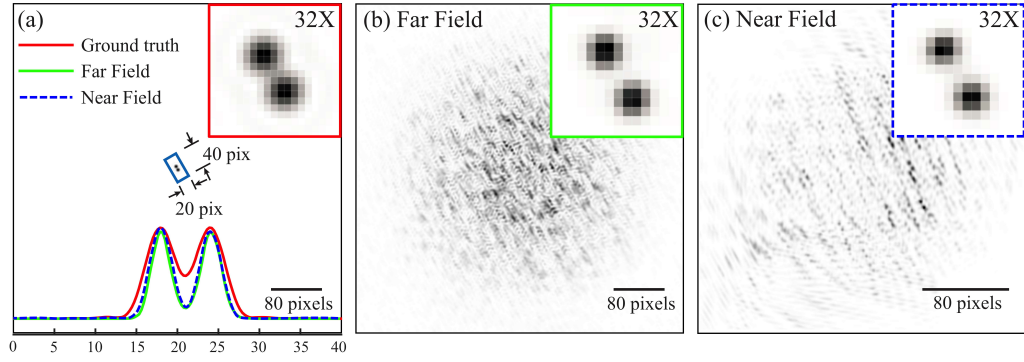
FIG. 7. Comparison of image reconstruction results of multi-frame blind deconvolution applied to a numerically simulated far field sequence and a near field sequence respectively(monochromatic). Both sequences are generated with $M = 50$ non-overlapping sub-apertures(or reflecting elements), and having random tip-tilt error of $\sigma_0 = 10\lambda/D$ and piston error of $\Delta z = 1\lambda$. Each sequence consists of $N \approx 60$ images. (a)Groundtruth image of the binary light sources, and the comparison of the line profile of the ground truth and the recovered results; (b)A typical far field image in the sequence, and enlarged part of recover result; (c))A typical near field image in the sequence, and enlarged part of recover result
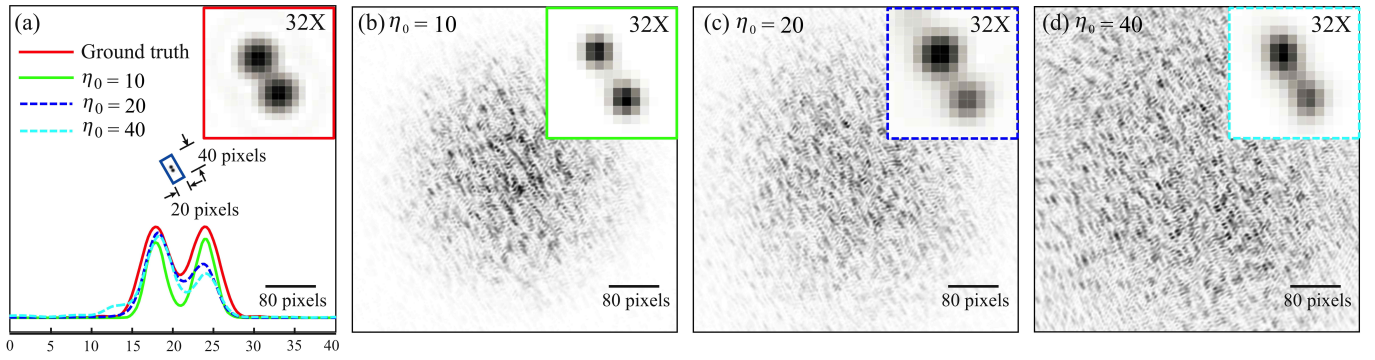

FIG. 8. Comparison of tip-tilt error to the image reconstruction results. Three monochromatic far field sequences are numerically simulated with $M = 100$ non-overlapping sub-apertures having random tilt-tilt error with σ_0 of 20, 40, and 60$[\lambda/D]$ respectively, and piston phase error with of $\Delta z = 1\lambda$. Each sequence consists of $N = 60$ images.(a)Groundtruth image of the binary light sources; (b)-(d) a typical image from each of the three sequences and enlarged part of its reconstruction result.
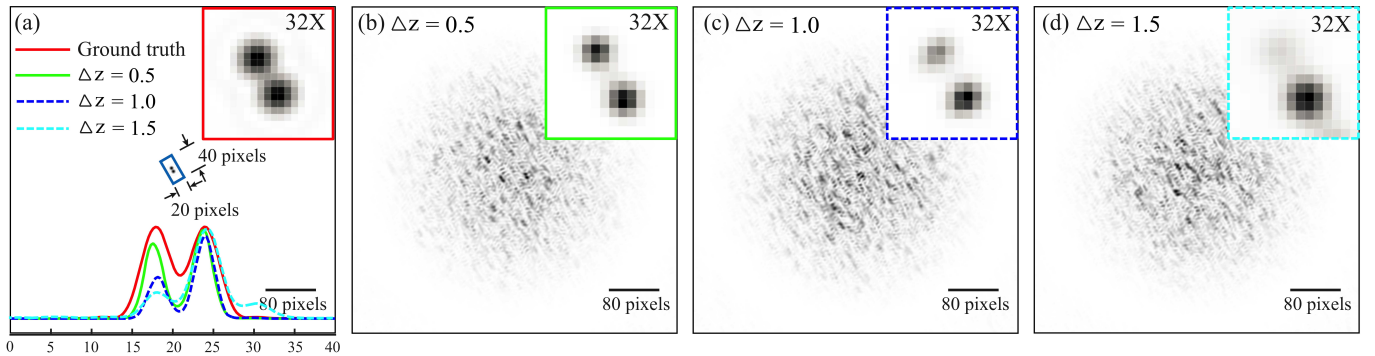

FIG. 9. Comparison of piston error to the image reconstruction results. Three monochromatic far field sequences are numerically simulated with $M = 100$ non-overlapping sub-apertures having random tilt-tilt error with $\sigma_0 = 40\lambda/D$, and piston phase error with $\Delta z = 0.5, 1.0, 1.5[\lambda]$ respectively. (a)Groundtruth image of the binary light sources, and comparison of line profile of the groundtruth and reconstructed results; (b)-(d)a typical image from each of the three sequences and enlarged part of its reconstruction result.

[8] A. L. Duncan, R. L. Kendrick, and R. D. Sigler, "Multi-aperture imaging system," (1999). US Patent 5,905,591.

[9] S.-J. Chung, D. W. Miller, and O. L. de Weck, "Design and implementation of sparse aperture imaging systems," in "Astronomical Telescopes and Instrumentation," (International Society for Optics and Photonics, 2002), pp. 181–192.

[10] N. J. Miller, M. P. Dierking, and B. D. Duncan, "Optical sparse aperture imaging," Applied Optics **46**, 5933–5943 (2007).

[11] M. Forot, P. Laurent, F. Lebrun, and O. Limousin, "Compton telescope with a coded aperture mask: Imaging with the integral/ibis compton mode," The Astrophysical Journal **668**, 1259 (2007).

[12] A. Haboub, A. MacDowell, S. Marchesini, and D. Parkinson, "Coded aperture imaging for fluorescent x-rays," Review of Scientific Instruments **85**, 063704 (2014).

[13] A. Bravin, P. Coan, and P. Suortti, "X-ray phase-contrast imaging: from pre-clinical applications towards clinics," Physics in medicine and biology **58**, R1 (2013).

[14] A. Kavanagh, A. Olivo, R. Speller, and B. Vojnovic, "Feasibility testing of a pre-clinical coded aperture phase contrast imaging configuration using a simple fast monte carlo simulator," Biomedical optics express **5**, 93–105 (2014).

[15] A. Veeraraghavan, A. Agrawal, A. Mohan, and J. Tumblin, "Dappled photography: Mask enhanced cameras for heterodyned light fields and coded aperture refocusing," (2007).

[16] P. Green, W. Sun, W. Matusik, and F. Durand, "Multi-aperture photography," in "ACM Transactions on Graphics (TOG)," , vol. 26 (ACM, 2007), vol. 26, p. 68.

[17] M. S. Asif, A. Ayremlou, A. Veeraraghavan, R. Baraniuk, and A. Sankaranarayanan, "Flatcam: Replacing lenses with masks and computation," .

[18] P. Hariharan, *Optical interferometry* (Academic press, 2003).

[19] É. Thiébaut, "Optimization issues in blind deconvolution algorithms," in "Astronomical Telescopes and Instrumentation," (International Society for Optics and Photonics, 2002), pp. 174–183.

[20] H. H. Bauschke, P. L. Combettes, and D. R. Luke, "Phase retrieval, error reduction algorithm, and fienup variants: a view from convex optimization," JOSA A **19**, 1334–1345 (2002).

[21] P. Ruiz, X. Zhou, J. Mateos, R. Molina, and A. K. Katsaggelos, "Variational bayesian blind image deconvolution: A review," Digital Signal Processing (2015).

[22] P. Tuthill, J. Lloyd, M. Ireland, F. Martinache, J. Monnier, H. Woodruff, T. ten Brummelaar, N. Turner, and C. Townes, "Sparse-aperture adaptive optics," in "SPIE Astronomical Telescopes+ Instrumentation," (International Society for Optics and Photonics, 2006), pp. 62723A–62723A.

[23] R. Fergus, A. Torralba, and W. T. Freeman, "Random lens imaging," (2006).

[24] Z. Zhang, P. Isola, and E. H. Adelson, "Sparkle vision: Seeing the world through random specular microfacets," arXiv preprint arXiv:1412.7884 (2014).

[25] S. M. Jefferies and J. C. Christou, "Restoration of astronomical images by iterative blind deconvolution," The Astrophysical Journal **415**, 862 (1993).

[26] S. Harmeling, M. Hirsch, S. Sra, and B. Scholkopf, "Online blind deconvolution for astronomical imaging," in "Computational Photography (ICCP), 2009 IEEE International Conference on," (IEEE, 2009), pp. 1–7.

[27] M. Hirsch, S. Sra, B. Scholkopf, and S. Harmeling, "Efficient filter flow for space-variant multiframe blind deconvolution," (2010).

[28] S. Kuwamura, Y. Azuma, N. Miura, F. Tsumuraya, M. Sakamoto, and N. Baba, "Multiframe blind deconvolution applied to diverse shift-and-add images of an astronomical object," Optical Review **21**, 9–16 (2014).

[29] G. Ayers and J. C. Dainty, "Iterative blind deconvolution method and its applications," Optics letters **13**, 547–549 (1988).

[30] X. Peng, G. J. Ruane, A. B. Artusio-Glimpse, and G. A. Swartzlander, "Image restoration from a sequence of random masks," in "IS&T/SPIE Electronic Imaging," (International Society for Optics and Photonics, 2015), pp. 94010D–94010D.

[31] M. Hirsch, S. Harmeling, S. Sra, and B. Schölkopf, "Online multi-frame blind deconvolution with super-resolution and saturation correction," Astronomy and Astrophysics-Les Ulis **531**, 1217 (2011).

[32] X. Peng, G. Swartzlander *et al.*, "Mirror swarm space telescope," in "Image and Signal Processing Workshop (WNYISPW), 2014 IEEE Western New York," (IEEE, 2014), pp. 37–41.